Application of Turbulence Models for Aerodynamic and Propulsion Flowfields

Linda D. Kral,* Mori Mani,† and John A. Ladd‡
McDonnell Douglas Aerospace, St. Louis, Missouri 63166

An evaluation of two algebraic models, two one-equation models, and six two-equation turbulence models is made for compressible flows encountered in current aircraft applications. A zonal, upwind, implicit, factored algorithm is used to solve both the mean flow equations and the turbulence model equations for three-dimensional, compressible turbulent flow. Calculations are presented for two transonic supercritical airfoils, a single-slot two-dimensional ejector nozzle, and a highly offset three-dimensional diffuser. The influence of two modifications to the production of turbulent kinetic energy for the low Reynolds number k–ϵ models is evaluated, a vorticity-based strain rate and a production limiter. The production limiter greatly improves the accuracy of the predicted flowfields. Comparisons of the results of the various turbulence models are made with experimental measurements. Significant differences are observed in the model predictions when applied to the same problem using the same computational mesh and mean flow solver. The algebraic models are unable to capture the physics of these complex flowfields, particularly for the internal flow calculations. Each one-equation and two-equation model has specific strengths and weaknesses and the performance of each model is assessed.

Nomenclature

C_f	= skin friction coefficient
C_p	= pressure coefficient
c	= chord length of airfoil
D	= diffuser diameter
D_k	= dissipation of turbulent kinetic energy
IDC_s	= simple distortion index
k	= turbulent kinetic energy
L	= characteristic length scale
L_D	= diffuser length
M	= Mach number
P	= pressure
P_k	= production of turbulent kinetic energy
$P_{t_{avg}}$	= average engine face total pressure
P_{t_∞}	= freestream total pressure
$P_{t_{max}}$	= maximum engine face total pressure
$P_{t_{min}}$	= minimum engine face total pressure
P_{t_p}	= primary flow total pressure
P_{t_p}/P_∞	= nozzle pressure ratio
P_{t_s}	= secondary flow total pressure
Pr	= Prandtl number
Pr_t	= turbulent Prandtl number
Re	= Reynolds number, $\bar{\rho}_\infty^* U_\infty^* L^*/\mu_\infty^*$
R_t	= turbulent Reynolds number, $\bar{\rho} k^2 Re/\bar{\mu} \epsilon$
s_{ij}	= strain rate tensor
T	= temperature
t	= time
U_∞	= freestream velocity
$\tilde{u}_j$	= velocity vector
x	= streamwise coordinate
y	= normal coordinate
y^+	= dimensionless distance from wall, $\bar{\rho}_w y u_\tau Re/\bar{\mu}_w$
z	= spanwise coordinate
$\Delta P/c_P$	= circumferential distortion intensity
$\Delta P/r_P$	= radial distortion intensity

ϵ	= turbulent energy dissipation rate
$\bar{\mu}$	= molecular viscosity
$\bar{\mu}_t$	= turbulent viscosity
$\bar{\nu}$	= kinematic viscosity
$\bar{\rho}$	= density
ω	= ϵ/k
$|\tilde{\omega}|$	= magnitude of the vorticity

Subscript

∞	= freestream condition

Superscripts

$^-$	= Reynolds averaged quantity
$^\sim$	= Favre averaged quantity
$*$	= dimensional quantity

I. Introduction

A LMOST all fluid flow problems involved in the design of today's high-performance aircraft involve turbulent flows. The computational storage and speed capabilities of current computers are inadequate to resolve all of the turbulent structures present in such flows. A model approximation to the flow turbulence is necessary in many applications to adequately simulate the performance parameters of interest. New methods of obtaining closure of the Favre-averaged Navier–Stokes equations are frequently being proposed. Two-equation turbulence models are conceptually better able to predict more complex turbulent flows than zero- and one-equation models since both the velocity and length scales are globally solved. One- and two-equation turbulence models employ the assumption that the Boussinesq approximation (which relates Reynolds stresses to the mean velocity strain) is valid and that the turbulence is isotropic. When this assumption is not valid, the calculation will be in error regardless of how accurately the model equations are solved. Reynolds stress transport models, which do not use the Boussinesq assumption, are considered to be too CPU intensive for most engineering calculations and have yet to be applied to many complex flows, particularly wall-bounded flows. Considering both accuracy and design cycle time, the two-equation model seems to be the highest-order model that can be used to solve the many complex problems encountered in aeronautical engineering.

Until recently, most applications in computational fluid dynamics (CFD) utilized either algebraic (or zero-equation) turbulence

models or the two-equation models. However, there has been a recent resurgence of one-equation models such as the Baldwin–Barth[1] (BB) and Spalart–Allmaras[2] (SA) models with very encouraging results.[3] Therefore, this investigation is focused on investigating the ability of algebraic, one- and two-equation turbulence models to accurately predict turbulent flows. Many formulations of one-equation and two-equation models have been proposed. These models are most frequently validated for simple canonical flows such as flat plates, channels, and free shear flows because much experimental data and direct numerical simulation data have been generated for these simple flowfields. Although these validations are essential, they do not necessarily show how the turbulence model will perform when extended to more complex problems. It is imperative that an evaluation of different turbulence models be performed for complex flows typically encountered in industry. Assumptions made in a turbulence model formulation may be entirely valid for simple two-dimensional flows, but may break down completely for more complex two- or three-dimensional flows. When this occurs there can be substantial errors in the prediction of both turbulent and mean flow properties.

To determine the applicability of the various turbulence models to a variety of practical problems, computations are presented for two Royal Airforce Establishment (RAE) transonic supercritical airfoils, a single-slot two-dimensional ejector nozzle, and a highly offset three-dimensional diffuser. The various turbulence models were chosen because of their widespread usage and/or their promise in predicting complex turbulent flows. Two algebraic models, the Baldwin–Lomax[4] (BL) wall model and the shear layer model of Thomas[5] (PDT), are investigated. The recent one-equation models of BB (Ref. 1) and SA (Ref. 2) are investigated. Five low Reynolds number k–ϵ models, the models of Jones and Launder[6] (JL), Chien[7] (CH), Speziale et al.[8] (SP), Coakley and Huang[9] (HC), and Zhang et al.[10] (SO), are evaluated in this work. The low Reynolds number form is chosen instead of the wall function approach because of its more rigorous near-wall treatment of turbulent quantities. Because of the recent success of the blended k–ω/k–ϵ shear-stress transport (SST) model of Menter,[11,12] this model is also included for evaluation. Of particular interest is the capability of the SST model for internal flows, since it has been primarily benchmarked for external aerodynamics. These turbulence models are introduced into the McDonnell Douglas Navier–Stokes solver, NASTD.[13]

The turbulence models and the associated model constants were developed primarily for incompressible boundary-layer flows, and it is not known a priori how the models will perform in compressible flows. The SO and HC two-equation models were specifically chosen for this investigation because the damping functions and low Reynolds number terms were developed for compressible flows. The three flowfields chosen for this study have also been previously investigated by Ladd and Kral.[14] Since this prior investigation, the two one-equation models, the SO and HC $k - \epsilon$ models and the SST k–ω/k–ϵ model, have been implemented and are evaluated here. Modifications to the production of turbulent kinetic energy in the two-equation k–ϵ models, based on a limiter used for the SST model, have also been introduced since the earlier study. These modifications greatly improve the turbulent flow predictions. The current investigations show detailed comparisons of the different turbulence models and the effect of the production limiter in the k–ϵ two-equation models for these flows.

II. Governing Equations and Solution Procedure

The governing equations for continuity, momentum, and energy are solved decoupled from the turbulence model. Ideal gas is assumed, and Sutherland's law is used for the molecular viscosity. A Prandtl number of $Pr = 0.72$ and a turbulent Prandtl number of $Pr_t = 0.9$ are used in the calculations. Details of the complete Navier–Stokes equations are presented in Bush,[13] and the governing equations for all of the turbulence models used in this work are presented in Kral et al.[15] A short description of the various turbulence models is given next.

The BL algebraic model[4] is one of the most widely used turbulence models by the CFD community. This model generally predicts external attached boundary-layer flows well, but is deficient for separated flows and for complex internal flows. The BL model is an

algebraic two-layer model with the turbulent eddy viscosity $\bar{\mu}_t$ given by a separate expression in each layer. The PDT algebraic model is an extension of the BL turbulence model to unbounded flows. The boundary-layer form of the BL model is used at the solid boundaries, but the eddy viscosity in the off-body flow is computed with the PDT model. In the PDT formulation, coordinate lines that are mainly perpendicular to the general fluid movement are divided into sections determined by the location of the flow boundaries, velocity maximum and minimums, and the vorticity distribution.

Recently, Baldwin and Barth[1] have developed a self-consistent one-equation model that avoids the need for algebraic length scales. Baldwin and Barth transformed the k–ϵ equations to avoid numerical difficulties. The BB one-equation model solves a partial differential equation over the whole field for the modified turbulent Reynolds number $\bar{\nu} \bar{R}_T$. Spalart and Allmaras,[2] on the heels of the success of the BB model, have developed a one-equation model. The SA model is not derived from the k–ϵ equations; it is generated from first principles. The motivation for this approach is that the BB model is constrained by the k–ϵ ancestry.

The k–ϵ two-equation turbulence model is widely used in CFD applications today. The JL[6] low Reynolds number model was one of the earliest k–ϵ models in which the equations are integrated directly to the wall, instead of using wall functions. In addition to the JL model, four additional low Reynolds number k–ϵ models are considered, the CH,[7] SP,[8] HC,[9] and SO[10] models. The constants and damping functions determine the form of each low Reynolds number model and are unchanged from those given in the original versions. A detailed comparison of the low Reynolds number model terms can be found in Kral et al.[15]

The production of turbulent kinetic energy (utilizing the Boussinesq approximation) can be written as

$$P_k = \bar{\mu}_t \left[\frac{1}{2} \left(\frac{\partial \bar{u}_i}{\partial x_j} + \frac{\partial \bar{u}_j}{\partial x_i} \right)^2 - \frac{2}{3} \left(\frac{\partial \bar{u}_k}{\partial x_k} \right)^2 \right] - \frac{2}{3} \bar{\rho} k \frac{\partial \bar{u}_k}{\partial x_k} \quad (1)$$

The exact term for the production P_k can cause unrealistically large values of eddy viscosity in stagnation regions because the normal stresses are not correctly predicted by the eddy viscosity approach in this region. Also, in regions of small values of ϵ/k, small disturbances in the shear strain rate can lead to erroneous spikes in the eddy viscosity in the freestream or near the boundary-layer edge.[12] In the development of the blended k–ω/k–ϵ model, Menter[12] has suggested a limiter on the production term for k given by the following formula:

$$\hat{P}_k = \min(P_k, 20 D_k) \quad (2)$$

where $D_k = \bar{\rho} \epsilon$ is the dissipation term. This limiter eliminates the unrealistic buildup of eddy viscosity in the stagnation regions of airfoils and removes the occurrence of spikes in the eddy viscosity resulting from numerical oscillations in the shear-strain tensor.[12] Menter carefully tested the limiter in the context of the blended k–ω/k–ϵ model. We tested the limiter for the low Reynolds number k–ϵ models using values of 10, 20, and 50 D_k and found no effect of the value of the coefficient on the airfoil solutions. The vorticity magnitude $|\bar{\omega}|$ has often been used to replace the strain rate $\bar{s}_{ij}$ in turbulence models:

$$\hat{P}_k = \bar{\mu}_t |\bar{\omega}|^2 \quad (3)$$

where

$$|\bar{\omega}| = \sqrt{\Omega_{ij} \Omega_{ij}}, \qquad \Omega_{ij} = \frac{\partial \bar{u}_i}{\partial x_j} - \frac{\partial \bar{u}_j}{\partial x_i}$$

$$\bar{s}_{ij} = \frac{1}{2} \left(\frac{\partial \bar{u}_i}{\partial x_j} + \frac{\partial \bar{u}_j}{\partial x_i} \right)$$

In this work, the algebraic and one-equation models both use the magnitude of the vorticity instead of the strain rate. The justification for the use of vorticity instead of the strain rate is that in most flows of interest, turbulence is found only where vorticity is present. However, there are regions of vorticity without turbulence behind shocks, but it is normally too weak to produce much eddy viscosity.

The vorticity, however, does not always give a physically realizable value, e.g., in flows with solid body rotation the strain rate is zero, but the vorticity will not be zero. An evaluation of the standard production term [Eq. (1)], the production limiter [Eq. (2)], and the use of vorticity in the production term [Eq. (3)] is made in this paper.

Menter[11,12] has developed a new version of the k–ω two-equation model that is designed to give results similar to those of Wilcox,[16] but without its strong dependency on arbitrary freestream values. The model is similar to the Wilcox model in the inner 50% of the boundary layer, but changes gradually to the high Reynolds number JL k–ϵ model (in a k–ω formulation) toward the boundary-layer edge. The new model is virtually identical to the JL model for free shear layers. The k–ϵ model is transformed into a k–ω formulation. The difference between this formulation and the original k–ω model is that an additional cross diffusion term appears in the ω equation. The modeling constants are also different than the original k–ω model. The SST model is a modified version of the baseline (BSL) Menter model that is designed to account for the transport of the principal turbulent stress and is evaluated in this work. Menter's limiter on the production term [Eq. (2)] is used in the SST model.

The solution methodology for the governing equations uses a zonal approach, which enables complex geometries to be broken down into smaller blocks. This approach allows an improved grid topology to be used locally and reduces the computer memory required. The zonal boundaries need not be point matched, and linear interpolation is used to couple characteristic values. The governing equations are solved using an upwind, implicit, approximately factored algorithm with an optional total variation diminishing operator.[13] It can be run in two or three dimensions for internal or external, subsonic, transonic, supersonic, or hypersonic viscous or inviscid flows. Details of the numerical approach, including initialization of the turbulence quantities and boundary conditions on the turbulence quantities for the one- and two-equation models can be found in Mani et al.,[3] Ladd and Kral,[14] and Kral et al.[15]

III. Results

Transonic Supercritical Airfoil

The transonic airflow over a two-dimensional airfoil provides a good test of the ability of a turbulence model to predict the boundary-layer development along a curved surface with both favorable and adverse pressure gradients including a shock wave. Two RAE 2822 airfoil cases are considered, cases 7 and 10 (Ref. 17). Separation occurs downstream of the shock wave in case 10 and provides a more stringent test for turbulence models. The first RAE 2822 airfoil case, case 7, is analyzed at $M_\infty = 0.725$, 2.55-deg angle of attack, and $Re = 6.5 \times 10^6$. The second RAE 2822 airfoil case, case 10, is analyzed at $M_\infty = 0.75$, 3.19-deg angle of attack, and $Re = 6.2 \times 10^6$. All eight turbulence models are evaluated. An adiabatic wall boundary condition is enforced on the airfoil surface. A C-grid is employed using 257 chordwise points and 73 points normal to the surface. The grid density was increased from the earlier study of Ladd and Kral[14] and convergence is achieved on the current grid where the first y^+ in the off-body mesh is an average of 0.5 over the airfoil surface. The far-field distance is at 50 chord lengths from the airfoil. This far-field boundary was moved until no impact on the converged solution was found. The experimental angle of attack is also corrected for wall-interference effects to 2.12 deg for case 7 and to 2.70 deg for case 10, as recommended in the experimental study. In the experiments, boundary-layer transition was tripped near the leading edge of the airfoil. However, the presence of the roughness may have had a strong local effect on the pressure distribution.[17] All calculations are run fully turbulent.

The influence of the freestream turbulence level and the method of calculation used for the production term in the k–ϵ equations are examined. The surface pressure for the CH k–ϵ model is shown in Fig. 1 with the corresponding experimental data[17] for case 7. The pressure coefficient C_p is shown using the CH k–ϵ turbulence model with three different methods of calculating the production term. The high value of the freestream eddy viscosity leads to a smeared shock and a high buildup of eddy viscosity in the stagnation region of the airfoil. These calculations used the exact equation for the production of turbulent kinetic energy, P_k, as given by Eq. (1);
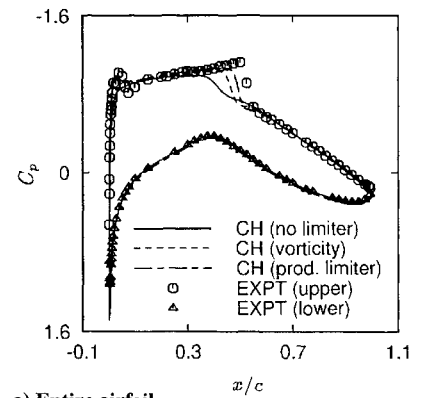
a) Entire airfoil
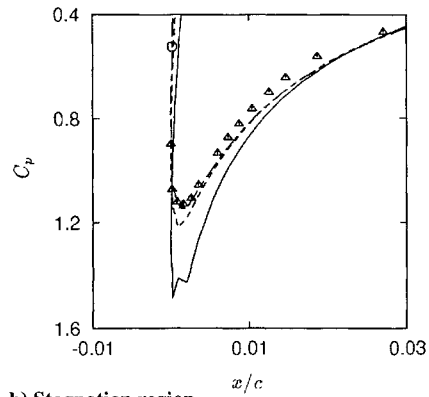
b) Stagnation region

Fig. 1 Effect of method of calculation of production on surface pressure coefficient C_p using the CH low Reynolds number k–ϵ turbulence model for a RAE transonic supercritical airfoil, case 7, for $\mu_{t_\infty}/\mu_\infty = 270$.
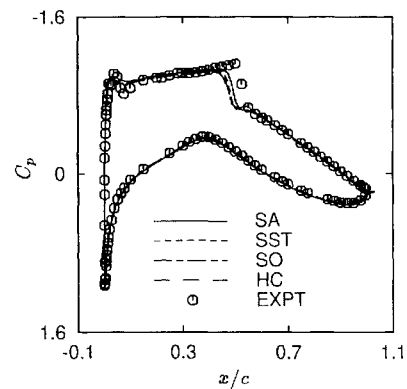

Fig. 2 Comparison with experiment of the variation of pressure coefficient C_p for a RAE transonic supercritical airfoil, case 7.

the vorticity magnitude replacing the strain rate, as given by Eq. (3); and the production limiter, as given by Eq. (2). The solutions using the vorticity magnitude show less of a freestream dependence on the eddy viscosity, although there is still a dependence at the highest value of $\bar{\mu}_t/\mu_\infty$ considered. The proposed production limiter has removed the artificial buildup of eddy viscosity in the stagnation region and greatly improved the flowfield prediction at the shock wave. Comparison for other models and freestream levels shows that the production limiter either equalled or improved the solution quality. Subsequent results reported here use this limiter, unless otherwise noted.
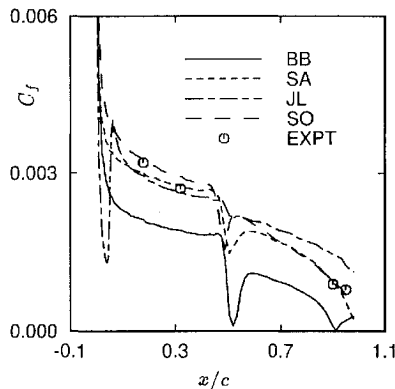
A comparison of the variation of the pressure coefficient C_p obtained using the SA one-equation model, the SO and HC low Reynolds number k–ϵ models, and the blended k–ω/k–ϵ model is shown in Fig. 2 for case 7. Overall, all of the models predict the location of the shock wave upstream of the experimental data (including the models not shown). The surface pressure predictions on the remainder of the airfoil all agree well with the data.

Table 1   Lift and drag coefficients for RAE airfoil: case 7, $M_\infty = 0.725$, $\alpha = 2.55$ deg

Model	C_D	% diff.	C_L	% diff.
Expt.	0.0107	——	0.658	——
BL	0.0114	+6.5	0.679	+3.2
BB	0.0090	−15.9	0.689	+4.7
SA	0.0116	+8.4	0.670	+1.8
SST	0.0110	+2.8	0.650	−1.2
CH	0.0123	+15.0	0.670	+1.8
JL	0.0110	+2.8	0.678	+3.0
SP	0.0124	+15.9	0.660	+0.3
SO	0.0113	+5.6	0.638	−3.0
HC	0.0121	+13.1	0.641	−2.6

Table 2   Lift and drag coefficients for RAE airfoil: case 10, $M_\infty = 0.75$, $\alpha = 3.19$ deg

Model	C_D	% diff.	C_L	% diff.
Expt.	0.0242	——	0.743	——
BL	0.0218	−9.9	0.735	−1.1
BB	0.0216	−10.7	0.739	−0.5
SA	0.0272	+12.4	0.777	+4.6
SST	0.0226	−6.6	0.720	−3.1
CH	0.0278	+14.9	0.781	+5.1
JL	0.0287	+18.6	0.781	+5.1
SP	0.0280	+15.7	0.787	+5.9
SO	0.0253	+4.5	0.741	−0.3
HC	0.0256	+5.8	0.742	−0.1

Fig. 3   Comparison with experiment of the variation of skin friction C_f for a RAE transonic supercritical airfoil, case 7.

Fig. 4   Comparison of velocity profiles for a RAE transonic supercritical airfoil, case 7, at $x/c = 0.9$.

The skin friction C_f on the upper surface is shown in Fig. 3 using the BB, SA, JL, and SO turbulence models compared with experimental data.[17] The experimental data shown were obtained from a Clauser fit to the velocity profile and are nondimensionalized by the boundary edge conditions, rather than the freestream conditions as for C_p. All models shown predict the skin friction very well before the shock wave. The skin friction downstream of the shock wave is best predicted by the SA one-equation model and the SO two-equation model. The JL two-equation model shows a reduction in skin friction near the leading edge of the airfoil, possibly indicating an initially laminar flow transitioning to fully turbulent flow. Other studies have shown that the JL model can predict transition and re-laminarization trends. The BB model is nearly separating aft of the shock wave and predicts too low of a skin friction. The predictions of the lift and drag coefficients, C_L and C_D, for each turbulence model and the experimental data are presented in Table 1. The drag includes both the viscous and form drag. Wide variations in the drag are predicted by the various turbulence models; particularly noticeable are the large variations among the two-equation models. The SST and JL two-equation models give the best predictions to within 3% of experiment. The BB one-equation model severely underpredicts the drag. The lift is predicted to within 3% by all models. An uncorrected angle of attack resulted in lift and drag coefficients in very poor agreement with the experiments. For example, the SA model showed a deviation in drag of +24% and a deviation from the experimentally determined lift of +14% without the correction.

Figure 4 shows the mean velocity profile for the SA, SST, SO, and HC models compared with experimental data downstream of the shock wave, at $x/c = 0.9$. The two-equation models are in the best agreement with the data.

RAE airfoil case 10 provides a more stringent test for turbulence models since the flow separates downstream of the shock wave. Figure 5 shows the variation of the pressure coefficient C_p for case 10 using the SA, SST, SO, and HC models. In contrast to case 7, the location of the shock wave found in the simulations is consistently aft of that found experimentally, with the SST model best predicting the shock wave location. The SA one-equation model best predicts the pressure downstream of the shock wave. The suction peak near
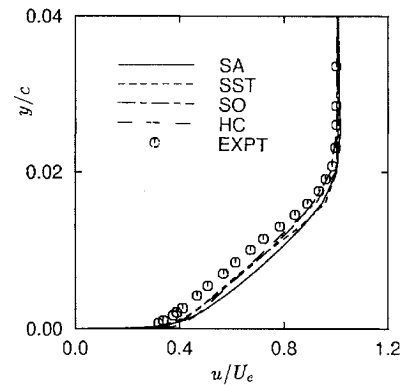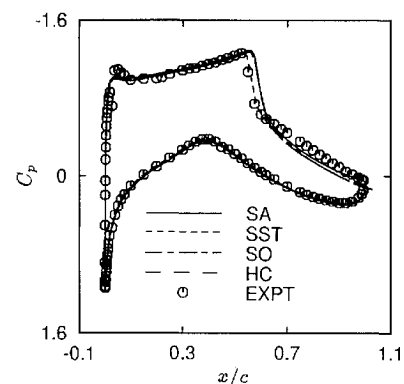
Fig. 5   Comparison with experiment of the variation of pressure coefficient C_p for a RAE transonic supercritical airfoil, case 10.

the leading edge of the airfoil is not predicted well by any model, which may be attributed to the effect of the roughness elements used to trip the boundary layer.

The skin friction on the upper surface of the airfoil for case 10 is shown in Fig. 6 using the SA, SST, SO, and HC models compared with experimental data.[17] As for case 7, the skin friction is predicted very well before the shock wave. The SST model gives the best overall prediction of skin friction before and aft of the shock wave. The predictions of the lift and drag coefficients, C_L and C_D, for case 10 are presented in Table 2 for all of the turbulence models. The drag predictions are best predicted by the SO and HC k–ϵ model predictions (to within 5%), and these models also show good agreement for the lift (to within 0.5%).

Figure 7 shows the mean velocity using the SA, SST, SO, and HC models compared with experiment aft of the shock wave, at $x/c = 0.750$. The SST model is in best agreement with the experimental data. In fact, only the SST model shows a separated velocity profile aft of the shock wave (including the models not shown), in better agreement with the experimental data.
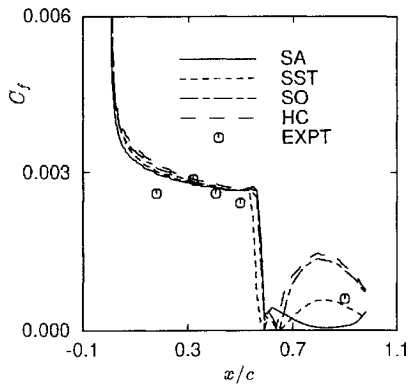
Fig. 6 Comparison with experiment of the variation of skin friction C_f for a RAE transonic supercritical airfoil, case 10.
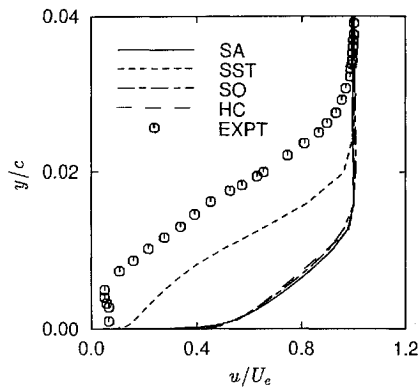

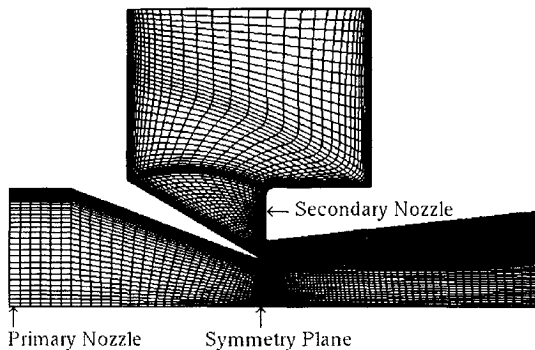Fig. 7 Comparison of velocity profiles for a RAE transonic supercritical airfoil, case 10, at $x/c = 0.750$.

Fig. 8 Four-zone computational grid for single-slot ejector nozzle.

Single-Slot Ejector Nozzle

Ejector nozzles are of interest because they can provide cooling air to heat sensitive surfaces. An ejector nozzle can be a demanding test of a turbulence model because multiple boundary layers and shear layers are present. An analysis of a multislot ejector nozzle using the PDT algebraic model and the JL k-ϵ model has previously been made by Ladd and Kral[18] and showed that the JL k-ϵ model yielded results of higher accuracy than the PDT algebraic shear layer model. Because this previous multislot ejector nozzle analysis involved 13 zones and over 50,000 grid points, a smaller test case of a single-slot ejector nozzle is considered here to evaluate the performance of the various turbulence models.

A four-zone computational mesh with over 17,000 grid points is employed for all calculations and is shown in Fig. 8. The zones are not point matched at the boundary near the nozzle throat, and there is a small base area where the primary and secondary flows come together in the throat region. A grid density study was performed, and all values of y^+ for the first grid point off the wall are less than 0.5.

The flow conditions are based on experiments for ejectors.[19] The conditions simulated are takeoff conditions at $T_\infty = 288$ K, $P_\infty = 101.4$ kPa, and a nozzle pressure ratio equal to 3.002. The total pressure ratio of the secondary flow to the primary flow P_{t_s}/P_{t_p} is 0.34, and the secondary weight flow ratio $\dot{m}_s/\dot{m}_p$ is 0.101.

The surface static pressure along the ejector is shown in Fig. 9 for the CH and HC k-ϵ models with the default calculation of the production and with the production limiter on. The addition of the production limiter has significantly improved the k-ϵ two-equation models results for the single-slot ejector nozzle, especially in the region of high flow curvature. The subsequent two-equation results are shown with the production limiter used.

The surface static pressure along the ejector is shown in Fig. 10 for all of the turbulence models. The PDT algebraic model, the BB and SA one-equation models, and the SST k-ω/k-ϵ two-equation model do not predict the static pressure as well as the k-ϵ two-equation models. None of the models is able to capture the pressure
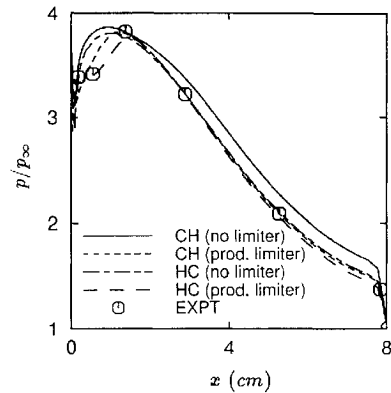

Fig. 9 Comparison with experiment of surface static pressure for a single-slot ejector nozzle using the production limiter for the CH and HC low Reynolds number k-ϵ turbulence models.
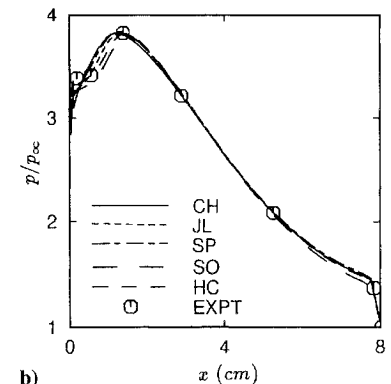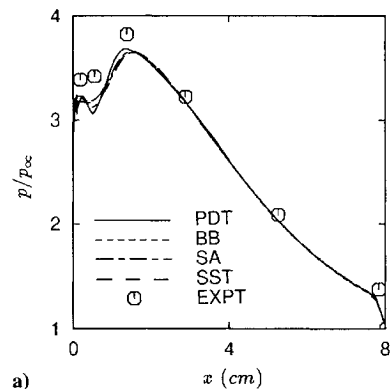

Fig. 10 Comparison with experiment of surface static pressure for a single-slot ejector nozzle using a) algebraic, one-equation, and SST turbulence models and b) low Reynolds number k-ϵ models.

distribution exactly in the throat region, but the k–ϵ models better predict the pressure in this area. This region is especially difficult for turbulence models because of the high curvature of the flow, high-pressure gradient, and flow separation. All models predict a separated flow, with the PDT and BB models predicting the largest amount of flow separation. The SO, HC, and SST models predict similar separation levels.

The ejector pumping is best predicted by the PDT algebraic model, followed by the HC two-equation model. All models predict a higher secondary air flow ratio than obtained experimentally. However, the k–ϵ two-equation models also predicted the most accurate variation of surface pressure in the supersonic region of the nozzle, and they are clearly better than an algebraic model for this flowfield in which multiple shear and boundary layers are present.

Highly Offset Three-Dimensional Diffuser

Successful computation of viscous turbulent flows in highly three-dimensional diffusers is very challenging. Accurate simulation of the flow turbulence can play a key role in successfully computing the pertinent performance parameters. Flow separations and large secondary flows in the duct create high demands on turbulence models.

The surface grid for the present diffuser is shown in Fig. 11 with the geometry shown on one side of the symmetry plane since only one side is actually computed. This diffuser has been analyzed in detail over a range of mass flow rates by Fletcher et al.[20] using the BL and BB turbulence models. Details of the experiments for this diffuser are also reported. Detailed attention was paid to grid topology and the computations compared favorably with the experiments.[20] The current study includes these two turbulence models in the evaluation. The diffuser has an area ratio of 1.6 and a L_D/D ratio of 4.5. The computational domain consists of four zone blocks: one zone external to the bellmouth with a grid density of $41 \times 41 \times 65$; an H-grid, which models the inboard part of the diffuser with grid density of $69 \times 61 \times 23$; and two polar grids, which resolve the more rounded outboard part of the diffuser (grid density of $69 \times 31 \times 21$) and the downstream diffuser (grid density of $69 \times 41 \times 65$). The grid is improved from the earlier simulations[14] and provides considerable axial grid clustering at the most significant parts of the diffuser, namely, the bellmouth entrance, diffuser throat, regions of high curvature, and the engine face station. Because of the large rate of flow curvature created by the offset, the boundary layer has a tendency to separate from the lower surface of the rear portion of the diffuser and so attention to grid clustering was made in this area. The average y^+ of the first grid point from the wall is 0.8. This high grid resolution is required to accurately assess differences between the turbulence model predictions so that differences are not a result of the computational grid. In the experiments, the model was tested with and without boundary-layer trips at the bellmouth entrance. Comparison is made here with the forced transition to enable direct comparison with the fully turbulent solutions. The freestream conditions are near static, and the flow through the diffuser is induced by specifying the experimental back pressure. The calculations
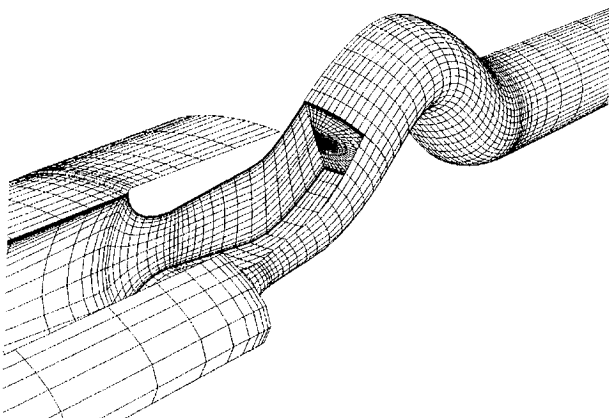
match the actual experimental mass flow rate of 1.336 kg/s (0.668 kg/s actually used because of the symmetry plane). To achieve a specified mass flow rate, the downstream pressure is automatically updated every 10 iterations based on the desired flow rate. The downstream pressure changes are monitored to ensure a converged solution.

The centerline pressure along the upper and lower surfaces of the diffuser is shown in Fig. 12 for the BL algebraic model, the BB and SA one-equation models, and the SST and SO two-equation models. The CH and JL models predict nearly identical behavior as the SO model and are not shown. The experimental data[21] are also shown. The predictions using the different turbulence models yield similar surface static pressure distributions and agree well with the data. The experimental pressure data are accurate to within less than ±0.2% (of full-scale values) on all measured and computed experimental parameters.[20] The computed surface pressure in the separated region aft of the lower surface turn is in greatest error. The BL algebraic model prediction is also in good agreement until this separated region. The characteristic flattening of the pressure on the lower surface is predicted best by the two one-equation models; however, the SA one-equation model predicts too large of a pressure decrease on the upper surface. The SST model also predicts a lower pressure than the other models downstream of the curved region on the upper surface because of the large flow separation predicted by this model. The numerical predictions appear to be shifted downstream by a constant streamwise spacing. Other analyses have shown similiar behavior possibly indicating an offset in the coordinates given in the experiments.

A comparison of the total pressure at the engine face using the various turbulence models and experimental data is shown in Fig. 13. The computational data are interpolated to the engine face rake probes, and a direct comparison is made with the experimental data. The standard 40 probe rake was used in the experiments as well as a 22.5-deg rotated rake, resulting in 80 total probe locations. The comparsion of total pressure is made for all 80 probes. The scale on the total pressure was clipped at $P_t/P_{t_\infty} = 0.85$ so that the variation in pressure at the engine face can be seen. The total pressure contours
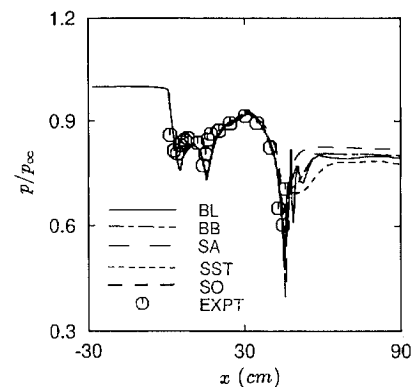

a) Upper surface
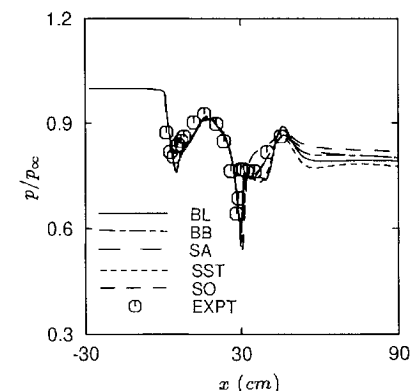
b) Lower surface

Fig. 12   Comparison with experiment of centerline pressure for a three-dimensional diffuser for different turbulence models.

Fig. 11   Computational grid for highly offset diffuser; every other grid point shown for clarity.

Table 3 Engine face recovery and distortion summary

Model	$P_{t_{avg}}/P_{t_\infty}$	$P_{t_{min}}/P_{t_\infty}$	IDC_s	$(\Delta P/r_P)_{max}$	$(\Delta P/c_P)_{max}$
Expt.	0.958	0.890	0.114	0.0141	0.0389
BL	0.945	0.714	0.304	0.0392	0.1017
BB	0.946	0.728	0.288	0.0272	0.1101
SA	0.956	0.855	0.153	0.0106	0.0661
SST	0.928	0.698	0.322	0.0484	0.1410
CH	0.970	0.901	0.102	0.0314	0.0430
JL	0.965	0.892	0.112	0.0274	0.0456
SO	0.976	0.893	0.108	0.0180	0.0467
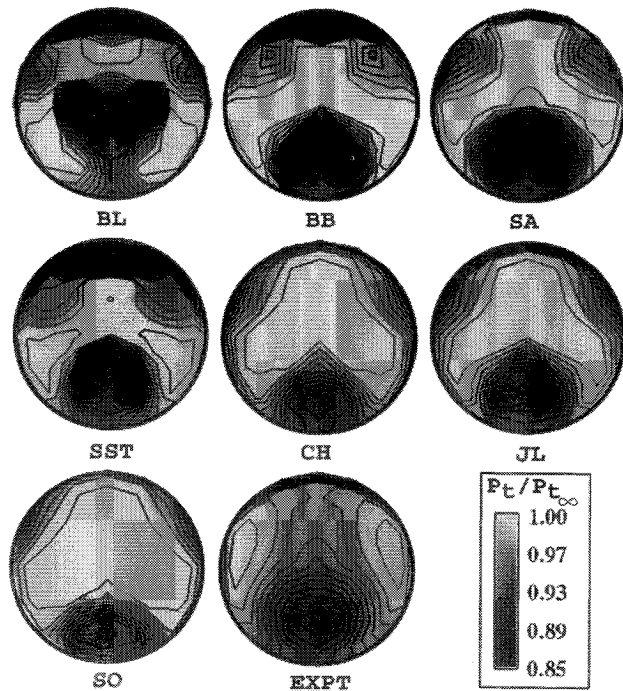
Fig. 13 Comparison of contours of the total pressure at the engine face ($x = 50.4$ cm) for a highly offset three-dimensional diffuser using various turbulence models.

are quite different between the models. The primary region of total pressure loss is similar but the deficit is greater and more clearly defined by the BL algebraic model, the BB and SA one-equation models, and the SST two-equation model. The losses do not diffuse as quickly for the BL, BB, SA, and SST models. The BL, BB, and SST models also predict a larger total pressure loss on the upper surface than that measured in the experiment because of the strong separation predicted by these models. The velocity profile for the $k-\epsilon$ and SA models remains attached, whereas all other models show a separated profile. The $k-\epsilon$ two-equation models yield a total pressure distribution at the engine face that more closely matches that obtained by experiment.

A summary of recovery and distortion data at the engine face is presented in Table 3 along with experimental data. The computational data are interpolated to the standard 40 engine face rake probes as well as the 22.5-deg rotated rake. The average between the recovery and distortion data on the standard rake and the rotated rake is tabulated. The simple distortion index IDC_s is defined by

$$IDC_s = \frac{(P_{t_{max}} - P_{t_{min}})}{P_{t_{avg}}}$$

The maximum radial distortion intensity $(\Delta P/r_P)_{max}$ and the maximum circumferential distortion intensity $(\Delta P/c_P)_{max}$ are computed using Society of Automotive Engineers Aerospace Information Report AIR 1419 standards.[22] The recovery parameters are best predicted by the two-equation models. The BL, BB, and SST models predict a very low minimum pressure at the engine face and very high engine face distortion because of the separation region predicted on the upper surface of the diffuser. The SA one-equation

model is in better agreement with the experimental data than the BL, BB, and SST models, but the CH, JL, and SO $k-\epsilon$ models more closely predict the recovery and distortion data at the engine face. The SO model is in closest agreement with the experimental data.

Overall, the $k-\epsilon$ two-equation models better predict the flow characteristics for the three-dimensional diffuser than the algebraic model, the one-equation models, and the SST model when compared with experimental data. The $k-\epsilon$ two-equation models better capture the physics of this diffuser flowfield and can be used to determine quantitative estimates of the diffuser performance parameters. Although the SST model overpredicted the separation on the upper surface of this highly curved diffuser, calculations of other offset diffuser configurations with smaller curvature have shown the SST model to predict the total pressure recovery very well. In another study using NASTD, the SST model has performed significantly better than the one-equation models and two-equation $k-\epsilon$ models for shock wave/turbulent boundary-layer interactions with strong separation present.[23]

Although accuracy in turbulent flow prediction is of extreme importance for aeronautical applications, design cycle time is also of high importance. The BB and SA one-equation models are the most computationally efficient models. Turbulent flow calculations using these models converge faster than even algebraic models because of the discontinuous eddy viscosity often calculated by algebraic models. The one-equation models are robust and CFL numbers as high as 10 have been used. The SST $k-\omega/k-\epsilon$ model is also computationally robust, with CFL numbers around 2.5 typically used. The computional cost is about 10% higher than that of the one-equation models. The $k-\epsilon$ two-equation models typically take two to seven times longer, depending on the application, for convergence than one-equation models primarily because of the lower CFL number requirements and the one additional equation that is solved. Although CFL numbers as high as 10 have been used for simpler flows, most complex flowfield applications require CFL numbers on the order of 1. For example, for the three-dimensional diffuser calculations, typically, around 10,000 iterations were run for the algebraic, one-equation, and SST models, whereas the $k-\epsilon$ models required between 25,000 and 50,000 iterations for convergence. The numerical procedure for the $k-\epsilon$ models is being modified to the same methodology as used for the SST model. The two-equation models are used in applications in which significant improvements are seen in the performance prediction or in final design studies.

IV. Summary

Several turbulence models have been examined for complex engineering flowfields. The BL and PDT algebraic models, the BB and SA one-equation models, the SST blended $k-\omega/k-\epsilon$ model, and the CH, JL, SP, HC, and SO low Reynolds number two-equation $k-\epsilon$ models have been evaluated for two RAE transonic supercritical airfoils, a single-slot ejector nozzle, and a highly offset three-dimensional diffuser.

Modifications to the production of turbulent kinetic energy for the two-equation $k-\epsilon$ models have also been evaluated. In one modification, the strain rate was replaced by the vorticity magnitude, and in the second modification, a limiter on the production was introduced based on the dissipation of turbulent kinetic energy. In a detailed analysis for the RAE airfoil, the computations were significantly improved by either modification, with the production limiter giving the best results. In addition, the ejector nozzle showed a significantly improved solution using the production limiter.

Overall, the two-equation models predicted turbulent flowfields better than the algebraic and one-equation models. The impact of the various turbulence models was not as significant for the RAE case 7 airfoil, but the RAE case 10 airfoil, with flow separation present, was best predicted by the SST model. The static surface pressure was improved in the ejector nozzle calculations using the two-equation $k-\epsilon$ models, with the HC model providing the best prediction. The engine face recovery parameters were significantly improved for the diffuser calculations using the $k-\epsilon$ two-equation models, with the SO and JL $k-\epsilon$ models giving the best prediction.

The algebraic models do not perform well in the internal flow applications where flow separation occurs. The BB one-equation model also does not perform as well as the SA one-equation model.

Overall, these calculations have shown that there is not a universal choice of the two-equation model. The SO k–ϵ model seems to consistently perform well for each application. In considering design cycle time, the most optimum choice of turbulence model is the SA one-equation model, followed by the SST model.

Acknowledgments

References

[1]Baldwin, B., and Barth, T. J., "A One-Equation Turbulence Transport Model for High Reynolds Number Wall-Bounded Flows," AIAA Paper 91-0610, Jan. 1991.

[2]Spalart, P. R., and Allmaras, S. R., "A One-Equation Turbulence Model for Aerodynamic Flows," AIAA Paper 92-0439, Jan. 1992.

[3]Mani, M., Wilhite, P., and Ladd, J. A., "Performance of One-Equation Models in CFD Applications," AIAA Paper 95-2221, June 1995.

[4]Baldwin, B., and Lomax, H., "Thin Layer Approximation and Algebraic Model for Separated Turbulent Flows," AIAA Paper 78-257, Jan. 1978.

[5]Thomas, P. D., "Numerical Method for Predicting Flow Characteristics and Performance of Nonaxisymmetric Nozzles, Part 2—Applications," NASA CR 3264, Oct. 1980.

[6]Jones, W. P., and Launder, B. E., "The Calculation of Low-Reynolds-Number Phenomena with a Two-Equation Model of Turbulence," International Journal of Heat and Mass Transfer, Vol. 16, 1973, pp. 1119–1130.

[7]Chien, K., "Prediction of Channel and Boundary Layer Flows with a Low Reynolds Number Turbulence Model," AIAA Journal, Vol. 20, No. 1, 1982, pp. 33–38.

[8]Speziale, C. G., Abid, R., and Anderson, E. C., "A Critical Evaluation of Two-Equation Models for Near Wall Turbulence," Inst. for Computer Applications in Science and Engineering, ICASE Rent 90-46, June 1990.

[9]Coakley, T. J., and Huang, P. G., "Turbulence Modeling for High Speed Flows," AIAA Paper 92-0436, Jan. 1992.

[10]Zhang, H. S., So, R. M. C., Speziale, C. G., and Lai, Y. G., "Near-Wall Two-Equation Model for Compressible Turbulent Flows," AIAA Paper 92-0442, Jan. 1992.

[11]Menter, F. R., "Improved Two-Equation k–ω Turbulence Models for Aerodynamic Flows," NASA TM 103975, Oct. 1992.

[12]Menter, F. R., "Zonal Two Equation k–ω Turbulence Models for Aerodynamic Flows," AIAA Paper 93-2906, July 1993.

[13]Bush, R. H., "A Three Dimensional Zonal Navier–Stokes Code for Subsonic Through Hypersonic Propulsion Flowfields," AIAA Paper 88-2830, July 1988.

[14]Ladd, J. A., and Kral, L. D., "Evaluation of Low-Reynolds-Number Two-Equation Turbulence Models for Calculation of Compressible Flows," Proceedings of the Symposium on Transitional and Turbulent Compressible Flows, edited by L. D. Kral and T. A. Zang, American Society of Mechanical Engineers, FED-151, 1993, pp. 159–174.

[15]Kral, L. D., Mani, M., and Ladd, J. A., "On the Application of Turbulence Models for Aerodynamic and Propulsion Flowfields," AIAA Paper 96-0564, Jan. 1996.

[16]Wilcox, D. C., "Reassessment of the Scale-Determining Equation for Advanced Turbulence Models," AIAA Journal, Vol. 26, No. 11, 1988, pp. 1299–1310.

[17]Fluid Dynamics Panel—Working Group 04, "Experimental Data Base for Computer Program Assessment," AGARD Advisory Rept. AR 138, Sept. 1979.

[18]Ladd, J. A., and Kral, L. D., "Development and Application of a Zonal k–ϵ Turbulence Model for Complex 3-D Configurations," AIAA Paper 92-3176, July 1992.

[19]Anon., private communication, General Electric, Schenectady, NY, 1990.

[20]Fletcher, M. J., Cosentino, G. B., Won, M. J., and Te, A., "Applying and Validating the RANS3D Flow Solver for Evaluating a Subsonic Serpentine Diffuser Geometry," AIAA Paper 93-2157, June 1993.

[21]Won, M. J., private communication, NASA Ames Research Center, Mountain View, CA, 1992.

[22]SAE Aerospace Council Division Technical Committee, "Inlet Total-Pressure-Distortion Considerations for Gas-Turbine Engines," Society of Automotive Engineers, SAE Aerospace Information Rept. AIR 1419, Warrendale, PA, May 1983.

[23]Donovan, J. F., "Control of Shock Wave/Turbulent Boundary Layer Interactions Using Tangential Injection," AIAA Paper 96-0443, Jan. 1996.